$Rb_4Ag_2BiBr_9$: A Lead-Free Visible Light Absorbing Halide Semiconductor with Improved Stability

Manila Sharma,[1‡] Aymen Yangui,[1‡] Vincent R. Whiteside,[2] Ian R. Sellers,[2] Dan Han[3,4,5],[†] Shiyou Chen[4], Mao-Hua Du,[5] Bayrammurad Saparov[1]*

[1]Department of Chemistry and Biochemistry, University of Oklahoma, 101 Stephenson Parkway, Norman, OK 73019, USA

[2]Homer L. Dodge Department of Physics & Astronomy, University of Oklahoma, 440 W. Brooks St., Norman, OK 73019, USA

[3]Key Laboratory of Polar Materials and Devices (Ministry of Education), East China Normal University, Shanghai 200241, China

[4]Department of Physics, East China Normal University, Shanghai 200241, China

[5]Materials Science and Technology Division, Oak Ridge National Laboratory, Oak Ridge, TN 37831, USA

[‡]These two authors contributed equally to this work.

[*]Corresponding authors: saparov@ou.edu

ABSTRACT. Replacement of the toxic heavy element lead in metal halide perovskites has been attracting a great interest because the high toxicity along with poor air stability are two of the major barriers for their widespread utilization. Recently, mixed-cation double perovskite halides, also known as elpasolites, were proposed as an alternative lead-free candidates for the design of non-toxic perovskite solar cells. Herein, we report a new nontoxic and air stable lead-free all-inorganic semiconductor $Rb_4Ag_2BiBr_9$ prepared using the mixed-cation approach; however, $Rb_4Ag_2BiBr_9$ adopts a new structure type (Pearson's code oP32) featuring $BiBr_6$ octahedra and $AgBr_5$ square pyramids that share common edges and corners to form a unique 2D layered non-perovskite structure. $Rb_4Ag_2BiBr_9$ is also demonstrated to be thermally stable with the measured onset decomposition temperature of T_o = 520 °C. Optical absorption measurements and density functional theory (DFT) calculations suggest a nearly direct band gap for $Rb_4Ag_2BiBr_9$. Room temperature photoluminescence (PL) measurements shows a broadband weak emission. Further, temperature-dependent and power dependent PL measurements show a strong competition between multiple emission centers and suggests the coexistence of defect-bound excitons and self-trapped excitons in $Rb_4Ag_2BiBr_9$.

INTRODUCTION

Metal halide perovskites have been at the forefront of solid state materials research in the past decade owing to their excellent optoelectronic, ferroelectric and semiconducting properties.[1-6] Among them, lead-based halide perovskites have been successfully incorporated into optoelectronic devices including solar cells with record efficiencies over 23%,[7] light-emitting diodes,[8,9] and ionizing radiation detectors.[10] The remarkable rise in power conversion efficiency allows consideration of Pb-based halide perovskite solar cells for commercialization, however, two obstacles remain: (i) the presence of the toxic heavy element Pb and (ii) poor stability of halide perovskites in a moist outdoor environment. In principle, altering the chemical composition and crystal structure of the absorber material should provide a solution to both of these critical concerns. Thus, a number of alternative non-Pb metal systems have been considered including the homovalent substitution of Pb^{2+} with Sn^{2+} and Ge^{2+}.[11-13] Despite some early success with Sn- and Ge-based compositions that resulted in fabrication of working solar cell devices based on $MASnI_3$ (where MA = CH_3NH_3),[12] the Sn- and Ge-based compositions are not actively considered for commercialization due to their extreme sensitivity to ambient air.[14]

The Bi^{3+} ion is isoelectronic with Pb^{2+}, therefore, a heterovalent substitution of Pb^{2+} with Bi^{3+} has also been explored in literature.[15] To preserve the charge balance, this substitution must be accompanied by further compositional changes such as in the cases of $MA_3Bi_2I_9$[16,17] which features a one-third Bi-deficient composition, and $Cs_2AgBiBr_6$[18,19] a double perovskite featuring Ag^+ and Bi^{3+} instead of Pb^{2+}. Metal deficient compositions such as $MA_3Bi_2I_9$ exhibit low-dimensional crystal structures (e.g., zero-dimensional (0D) "molecular" or two-dimensional (2D) layered perovskite structures depending on the metal and halide combinations) and therefore, generally have larger band gaps and poorer electronic transport properties.[20] In comparison, the emergence of the elpasolite-type double perovskites Cs_2AgBiX_6 (X = Cl, Br) was a major breakthrough because (i) the three-dimensional (3D) connectivity of metal halide network is preserved in these compounds and (ii) the all-inorganic compositions are expected to be more stable.[9,21-23] However, further experimental and computational investigations revealed that Cs_2AgBiX_6 have larger indirect band gaps above 1.9 eV[24-26] making their implementation in solar cells challenging. Moreover, very recently R. Kentsch et al.[27] investigated the excitons mechanisms on the halides double perovskite $Cs_2AgBiBr_6$ using femtosecond laser spectroscopy. They reported the presence of a very high exciton binding energy and strong electron-phonon coupling similarly to the case of $Cs_3Bi_2Br_9$ and $BiBr_3$, which induce unwanted electron-hole recombination and hamper carrier transport, and thus clearly limit their applicability in perovskite solar cells. Therefore, a new strategy is required for efficient carrier extraction at the interfaces of the double halide perovskite with electron and hole transport layers. The over-arching conclusion from the work on Bi-based Cs_2AgBiX_6 double perovskites is that the search for nontoxic Bi compositions must expand to other structure types.[26]

Despite the challenges associated with using Cs_2AgBiX_6 in solar cells, these materials have recently been incorporated into X-ray detectors with low detection limit and high X-ray stability.[28-29] Particularly advantageous properties of $Cs_2AgBiBr_6$ for radiation detection applications include the presence of heavy elements with the average Z value of 53.1,[29] long carrier lifetimes due to the indirect band gap and higher resistivity that yields reduced noise current.[28-30]

Here, we report a new nontoxic Bi-based all-inorganic semiconductor $Rb_4Ag_2BiBr_9$. Similar to the Pb-based halide perovskites, $Rb_4Ag_2BiBr_9$ can be conveniently obtained as large crystals measuring up to 1 cm in length using solution-based approaches. To the best of our knowledge, $Rb_4Ag_2BiBr_9$ is the first compound discovered in the quaternary Rb-Ag-Bi-Br phase diagram.

$Rb_4Ag_2BiBr_9$ adopts a new structure type (Pearson's code *oP*32) featuring $BiBr_6$ octahedra and $AgBr_5$ square pyramids that share common edges and corners to form a 2D layered non-perovskite structure. However, there are elongated interlayer Ag-Br contacts, which complete the octahedral coordination around Ag atom, leading to a quasi-3D structure of the compound. Our thermal and air stability tests revealed that $Rb_4Ag_2BiBr_9$ is stable in ambient air for weeks and has also improved thermal stability with an onset decomposition temperature of T_o = 520 °C. Photoluminescence (PL) measurements show a broadband emission composed of several sub-bands. Further, temperature-dependent and power-dependent PL measurements show a strong competition between multiple emission centers suggesting the coexistence of bound excitons and self-trapped excitons. Density functional theory (DFT) calculations performed on this compound show that it provides a nearly direct band gap of 1.69 eV (less than 0.01 eV difference between the direct and indirect band gaps) and flat bands near the Fermi level consistent with its low dimensional crystal structure. We discuss the potential of $Rb_4Ag_2BiBr_9$ and its substitution derivatives for optoelectronic applications based on our combined experimental and theoretical results.

EXPERIMANTAL SECTION

Chemicals. All chemicals used in this study were either used as purchased or synthesized from the starting materials listed: (i) rubidium bromide, 99.8%, Alfa Aesar; (ii) bismuth(III) bromide, anhydrous, powder, 99.998% trace metals basis, Sigma Aldrich (iii) hydrobromic acid, 48 wt. % in H_2O; (iv) silver nitrate, Sargent-Welch; (v) potassium bromide, Fisher Scientific.

Synthesis of $Rb_4Ag_2BiBr_9$. All synthetic preparations were carried out in air. Polycrystalline AgBr was precipitated from stoichiometric amounts of as prepared aqueous solutions of $AgNO_3$(aq) and KBr(aq). The resulting solid was filtered out and then dried under vacuum overnight under inert atmosphere. $Rb_4Ag_2BiBr_9$ single crystals were grown through slow evaporation of a stoichiometric solution containing a 4:2:1 molar ratio of RbBr:AgBr:$BiBr_3$ reactants in hydrobromic acid, 48 wt. % in H_2O. The solution synthesis experiment was carried out in a small vial (20 mL) at 90 °C for 1 hour. The $Rb_4Ag_2BiBr_9$ single crystals formed as large (up to 1 cm in length) yellow colored blocks in hours (see Figure S1(a) in the Supporting Information file (SI)). Crystals were also grown at a higher temperature of 130 °C; however, the quality of crystals produced were generally poorer compared to the low temperature growth described above.

Microscopy. Single crystals of $Rb_4Ag_2BiBr_9$ are shown in Figure S1(a), which was taken using a Leica S6D microscope equipped with a EC4 camera. Energy Dispersive X-ray (EDX) spectroscopy measurements were run on a Zeiss Neon EsB equipped with an Oxford Instruments EDX system. Elemental analysis of $Rb_4Ag_2BiBr_9$ crystals yields an average composition of 26.45% of Rb, 11.95% of Ag, 5.85% of Bi, and 55.75 % of Br, which present a good agreement with the calculated values; 25% of Rb, 12.5% of Ag, 6.25% of Bi, and 56.25% of Br (see Figure S1(b)).

Single crystal X-ray diffraction. Single crystal X-ray diffraction (SXRD) data were collected on a Bruker D8 Quest with a Kappa-geometry goniometer, an Incoatec Imus X-ray source (graphite-monochromated Mo-Kα (λ = 0.71073 Å) radiation), and a Photon II detector. The data were corrected for absorption using the semi-empirical method based on equivalent reflections and the structure was solved by intrinsic phasing methods (ShelXT) as embedded in the APEX3 v2016.9.0 program.[31] All atoms were refined with anisotropic displacement parameters. Site occupancy factors were checked by freeing occupancies of each unique crystallographic site. In the last refinement cycle, the unit cell axes and the atomic coordinates were standardized using the software STRUCTURE

TIDY.[32] Details of the data collection and crystallographic parameters are given in Table 1. Atomic coordinates, equivalent isotropic displacement parameters, and selected interatomic distances and bond angles are provided in Tables S1 and S2 in the SI. Additional information on the crystal structure investigations at room temperature can be obtained in the form of a CIF (Crystallographic Information File), which was deposited in the Cambridge Crystallographic Data Centre (CCDC) database (deposition number 1871838).

Powder X-ray diffraction. Powder X-ray diffraction (PXRD) measurements were carried out at room temperature on a Rigaku MiniFlex600 system equipped with a D/tex detector using Ni-filtered Cu-Kα radiation source. Typical PXRD scans were collected in the 3-90° (2θ) range, with a step size of 0.2° to determine phase identity and purity. The collected data were fitted using the decomposition method (also known as Pawley fitting) as embedded in Rigaku's PDXL2 software package.[33] To study the air stability of the $Rb_4Ag_2BiBr_9$, the sample was left in ambient air on a laboratory bench for 23 days and PXRD was measured periodically under the same conditions as described above.

Table 1. Selected room temperature single crystal data and structure refinement parameters for $Rb_4Ag_2BiBr_9$

Formula	$Rb_4Ag_2BiBr_9$
Formula weight (g/mol)	1485.79
Temperature (K)	298(2)
Radiation, wavelength (Å)	Mo Kα, 0.71073
Crystal system	Orthorhombic
Space group, Z	*Pnnm*, 2
Unit cell parameters (Å)	a = 8.4426(6)
	b = 12.9149(8)
	c = 9.9572(7)

Volume (Å^3)	1085.69(13)
Density (ρ_{calc}) (g/cm^3)	4.545
Absorption coefficient (μ) (mm^{-1})	35.318
$\theta_{\mathrm{min}} - \theta_{\mathrm{max}}$ (°)	2.58 – 36.24
Reflections collected	14815
Independent reflections	1370
R^a indices ($I > 2\sigma(I)$)	$R_1 = 0.0277$ $wR_2 = 0.0463$
Goodness-of-fit on F^2	1.088
Largest diff. peak and hole (e$^-$/Å^3)	1.141 and -1.688

$^a R_1 = \sum||F_o| - |F_c||/\sum|F_o|$; $wR_2 = |\sum|w(F_o^2 - F_c^2)^2|/\sum|w(F_o^2)^2||^{1/2}$, where $w = 1/|\sigma^2 F_o^2 + (AP)^2 + BP|$, with $P = (F_o^2 + 2F_c^2)/3$ and weight coefficients A and B.

Thermogravimetric Analyses. Thermogravimetric analysis (TGA) of the polycrystalline powder of $Rb_4Ag_2BiBr_9$ were performed using a TA Instruments SDT 650 thermal analyzer system. The sample was heated at a rate of 10 °C/min from 25 °C to 1300 °C under an inert flow of dry nitrogen gas.

Optical measurements. Room temperature diffuse reflectance spectrum was measured on a polycrystalline powder sample of $Rb_4Ag_2BiBr_9$ using a high-resolution PerkinElmer LAMBDA 750 UV–Vis–NIR spectrometer equipped with a 100 mm InGaAs integrating sphere attachment. Photoluminescence excitation (PLE) measurements were performed at ambient temperature using a HORIBA Jobin Yvon Fluorolog-3 spectrofluorometer equipped with a Xenon lamp and Quanta-φ integrating sphere. Temperature dependence and power dependence PL measurements were done on single crystals of $Rb_4Ag_2BiBr_9$ under excitation by the 325 nm line of a HeCd laser (Kimmon Electric HeCd dual-wavelength laser, model: IK552R-F). The sample was placed on the cold finger of a helium closed-cycle cryostat and the measurements were performed from 4 to 295 K.

Electronic structure calculations. All calculations were based on density functional theory (DFT) implemented in the VASP code.[34] The interaction between ions and electrons was described by projector augmented wave method.[35] The kinetic energy cutoff of 350 eV for the plane-wave basis was used. Experimental lattice parameters were used while the atomic positions were fully relaxed until the residual forces were less than 0.01 eV/ Å. The electronic band structure and density of states (DOS) were calculated using Perdew−Burke−Ernzerhof (PBE) exchange-correlation functional.[36] Spin-orbit coupling (SOC) was included.

RESULTS AND DISCUSSION

Crystal structure description. $Rb_4Ag_2BiBr_9$ crystallizes in the centrosymmetric space group *Pnnm* (No. 58) with seven crystallographically unique atoms in the asymmetric unit. Following the differences in electronegativity between the constituent elements, the structure of $Rb_4Ag_2BiBr_9$ can be rationalized as polyanionic $[Ag_2BiBr_9]^{4-}$ layers stacked along the *a*-axis and Rb^+ cations filling the interlayer space (Figure 1). The alternating polyanionic $[Ag_2BiBr_9]^{4-}$ layers along the *a*-axis are identical; neighboring anionic layers are inverted and shifted by half a unit cell along the *b*- and *c*-axes with respect to each other. The polyanionic $[Ag_2BiBr_9]^{4-}$ layer itself is formed by square pyramidal $AgBr_5$ and octahedral $BiBr_6$ building blocks. Thus, there are $[Ag_2Br_5]$ chains containing edge- and corner-shared $AgBr_5$ square pyramids extending along the *b*-axis, which are stitched along the *c*-axis by corner sharing $BiBr_6$ octahedra to yield the polyanionic $[Ag_2BiBr_9]^{4-}$ layers.

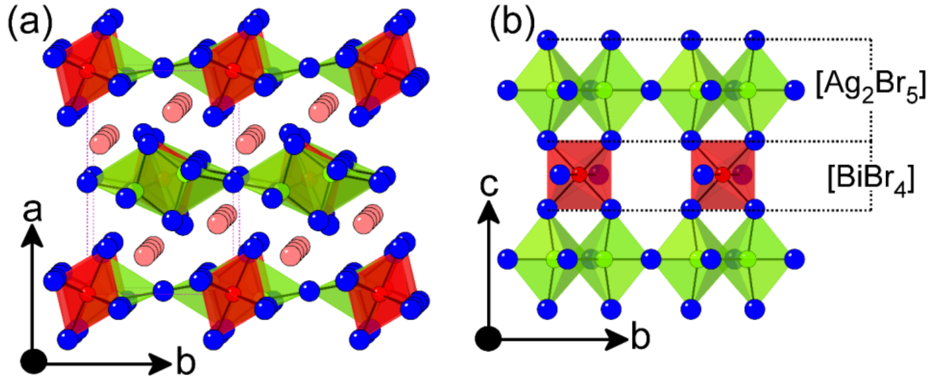

Figure 1. (a) A polyhedral representation of the crystal structure of $Rb_4Ag_2BiBr_9$ showing alternating polyanionic $[Ag_2BiBr_9]^{4-}$ layers stacked along the *a*-axis. (b) A top view of a segment of a $[Ag_2BiBr_9]^{4-}$ layer, which is composed of alternating $[Ag_2Br_5]$ and $[BiBr_4]$ slabs. The $[Ag_2Br_5]$ chain contains edge- and corner-shared $AgBr_5$ square pyramids, and are stitched along the *c*-axis by corner-shared $BiBr_6$ octahedra to yield the polyanionic $[Ag_2BiBr_9]^{4-}$ layers.

Coordination environments around metal cations are noticeably different in $Rb_4Ag_2BiBr_9$ compared to the ABX_3 perovskite structure that features large A cations in the cubooctahedral environment (with coordination number (CN) of 12) and smaller B cations in the octahedral environment (CN = 6). Here, the large interlayer cation Rb sits in a distorted square antiprism made of Br atoms (CN = 8); whereas, Ag and Bi have square pyramidal (CN = 5) and octahedral (CN = 6) environments, respectively (Figure 2). The $BiBr_6$ octahedra are almost regular with measured Bi–Br bond distances of 2.8582(5) – 2.8616(6) Å and Br–Bi–Br bond angles of 89.08(2) – 90.92(2)°, which suggests that the lone pair on Bi^{3+} cations are stereochemically inactive. Regular octahedra and a similar Bi–Br bond distance of 2.8678(14) Å has also been reported for the cubic hybrid organic-inorganic double perovskite $MA_2AgBiBr_6$. [37]

In contrast, the all-inorganic double perovskite $Cs_2AgBiBr_6$ features a slightly shorter Bi–Br bond distance of 2.813(5) – 2.8224(5) Å.[19,30] However, the difference is more apparent in the coordination environments of Ag in $Rb_4Ag_2BiBr_9$ and double perovskites $MA_2AgBiBr_6$ and $Cs_2AgBiBr_6$; while cubic double perovskites feature regular $AgBr_6$ octahedra with Ag–Br bond distances of 2.8025(4) – 2.822(5) Å in $Cs_2AgBiBr_6$[19,30] and 2.9507(14) Å in $MA_2AgBiBr_6$, the $AgBr_5$ square pyramids in $Rb_4Ag_2BiBr_9$ are noticeably distorted with Ag–Br bond distances ranging from 2.7127(9) to 3.0145(6) Å. The distortion of $AgBr_5$ square pyramids is also apparent from the Br–Ag–Br bond angles that include 83.57(2), 92.65 (2) and 153.21(3)° (see Table S2).

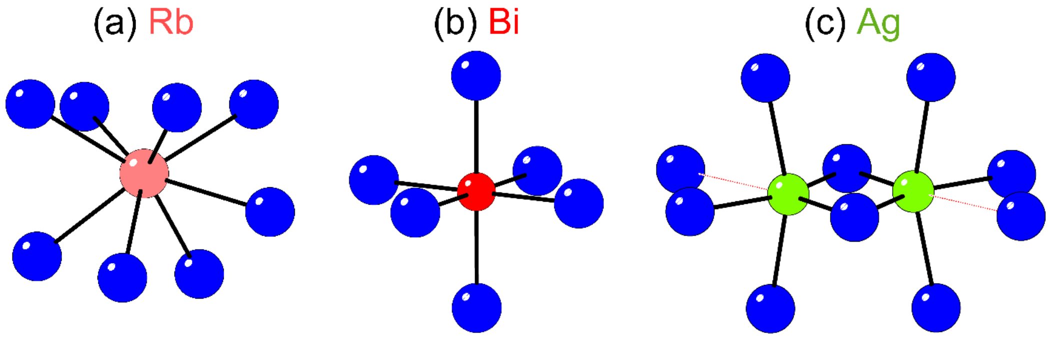

Figure 2. Coordination environments of metals in $Rb_4Ag_2BiBr_9$: (a) Rb occupies a distorted square antiprismatic coordination environment, (b) Bi has an octahedral coordination environment, and (c) Ag has a square pyramidal coordination environment. An additional elongated contact (shown using red dots) is present, yielding an overall octahedral coordination environment for Ag. Blue, pink, red, and green spheres in the structures represent Br, Rb, Bi, and Ag atoms respectively.

A closer inspection of the coordination environment of Ag reveals that there are elongated interlayer Ag–Br contacts at 3.6801(9) Å that complete the coordination environment of Ag to octahedral (Table S2). If an octahedral coordination around Ag is assumed, the structure of $Rb_4Ag_2BiBr_9$ becomes 3D similar to that in the double-perovskite structure (Figures S2 and S3 in the SI). However, the interlayer Ag–Br distance of 3.6801(9) Å considerably exceeds the sum of the Shannon ionic radii (3.11 Å) of Ag^+ (1.15 Å) and Br^- (1.96 Å) ions.[38] Indeed, Ag–Br distances are less than 3.11 Å in other reported all-inorganic Ag-Bi-Br compositions such as $Ag_3Bi_{14}Br_{21}$[39] and hybrid organic-inorganic compounds such as $K[TM(2,2\text{-bipy})_3]_2Ag_6Br_{11}$ (where TM = Ni, Co, Zn, Fe).[40] Therefore, based on XRD studies, the coordination polyhedron around Ag is assigned to be square pyramidal and the structure of $Rb_4Ag_2BiBr_9$ is 2D layered.

Stability studies. Figure 3 shows a comparison between the PXRD pattern of polycrystalline powder of $Rb_4Ag_2BiBr_9$ and the calculated pattern based on the single crystal structure diffraction data obtained at room temperature. The described synthetic procedure yields a phase pure product as judged by the clear match with the simulated single crystal data (Figure S4 in the SI). The unit cell parameters were refined to a = 8.4307(2) Å, b = 12.9105(3) Å, c = 9.9576(2) Å and V =1083.84(4) Å^3 with a reliability factor of Rp = 3.29% (weighted R-factor wRp = 4.58%) and S (goodness-of-fit) = 1.99133. Moreover, it is worth noting that the studied polycrystalline powder of $Rb_4Ag_2BiBr_9$ shows a good stability in air for several weeks (Figure 3). Although we carried out periodic PXRD measurements for only 3-4 weeks, no $Rb_4Ag_2BiBr_9$ sample decomposition or degradation was observed for the duration of this study (> 10 months).

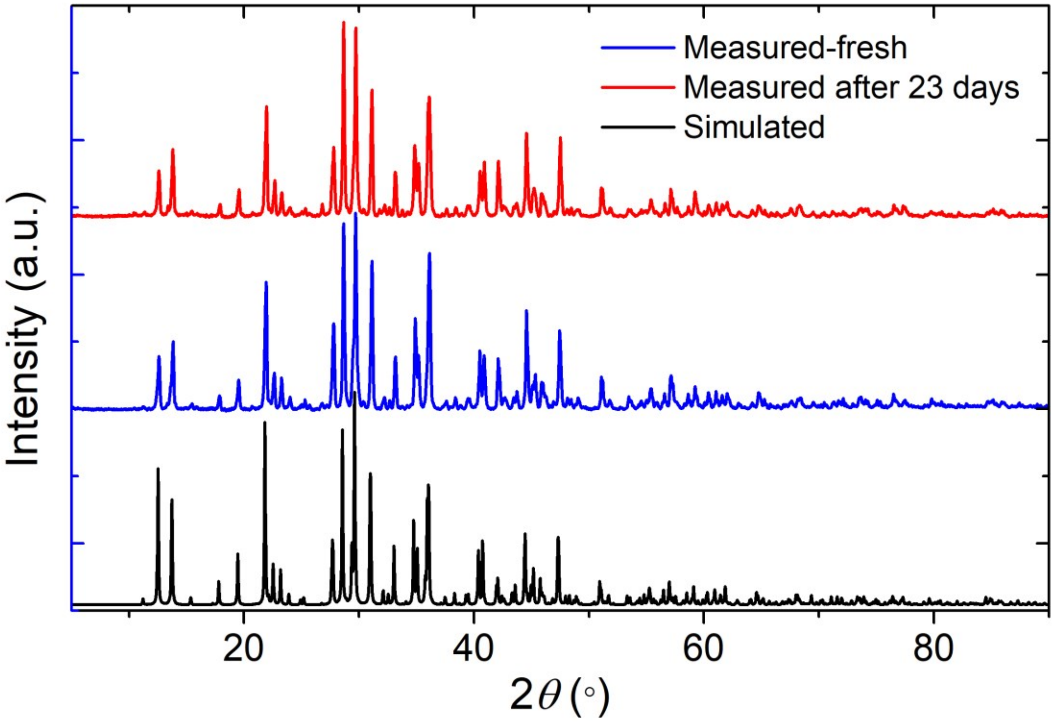

Figure 3. Comparison between the calculated PXRD pattern based on SXRD data (black) and the experimental PXRD patterns of polycrystalline powder of $Rb_4Ag_2BiBr_9$ measured on fresh sample (blue) and after 23 days (red).

It is well known that another major challenge for the commercialization of $CH_3NH_3PbI_3$-based solar cells is its poor thermal stability.[41-45] A potential solution for this problem is using all inorganic compositions, which are expected to exhibit higher stability owing to the lack of volatile organic molecules.[46-47] To investigate the thermal stability of the all-inorganic $Rb_4Ag_2BiBr_9$, we carried out TGA measurements. The results shown in Figure 4 confirm that the sample is stable up to 500 °C. The compound demonstrates a two-step decomposition profile. In the first step, the decomposition of the compound starts at the onset temperature of T_o = 520° C and ends with the end-set temperature T_e = 668 °C. After the first decomposition step, the leftover material corresponds to ~70% of the initial sample weight. The leftover weight suggests that 30% of the total weight lost in decomposition is 445.74, which is very close to molar mass of $BiBr_3$ (448.71 $g.mol^{-1}$). In the second step, the remaining mixture, which is likely composed of AgBr and RbBr, is evaporated upon heating. Therefore based on our TGA results, the thermal stability of $Rb_4Ag_2BiBr_9$ is much higher than the hybrid perovskite $MAPbBr_3$, which has a decomposition temperature of 176 °C,[37] and the related all-inorganic double halide perovskite $Cs_2AgBiBr_6$, which is reported to have a decomposition temperature of 430 °C.[30]

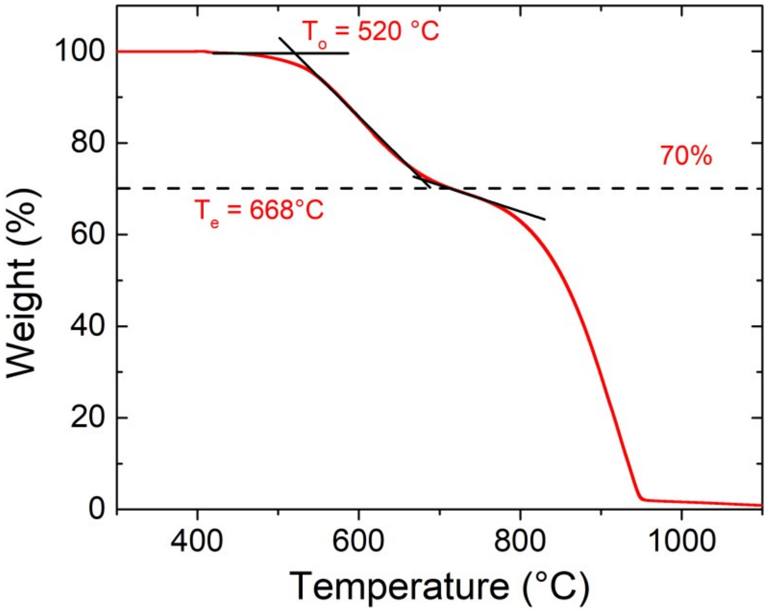

Figure 4. Thermogravimetric Analysis (TGA) data for a powder sample of $Rb_4Ag_2BiBr_9$.

Optical properties. The photophysical properties of $Rb_4Ag_2BiBr_9$ were investigated using diffuse reflectance, PLE and PL spectroscopies. The diffuse reflectance data (shown in Figure S5 in the SI) were transformed to pseudoabsorption data using the Kubelka-Munk function (F(R)), shown in Figure 5. This expresses the absorbance as a function of reflectance: $F(R) = \alpha/S = (1-R)^2/(2R)$, where R is the reflectance, α is the absorption coefficient, S is the scattering coefficient.[48] The F(R) plot (Figure 5a) shows the presence of well-defined absorption features at 2.82 and 3.23 eV. We noted that the shape of the F(R) absorbance plot (tails off gradually to lower energies) is similar to the case of most all-inorganic halide double perovskite reported up to date,[19, 30, 49-50] which is probably due to a high defect concentration, causing a Moss-Burstein shift of the band edge.[51-52] Usually, the Tauc plots are then calculated based on Kubelka-Munk transformed data presented in Figure 5 to estimate an optical band gap of a given material with parabolic bands at the Fermi energy level. Such procedure utilizes the equation $[F(R)h\nu]^{1/\gamma}$ vs the photon energy ($h\nu$), where γ is equal to 1/2 for direct transitions and 2 for indirect transitions.[53] Using the direct and indirect fitting scenarios, band gaps energies of 2.38 (indirect) and 2.57 eV (direct) are estimated for $Rb_4Ag_2BiBr_9$ (Figures S5b). These band gap values fall within the range of typical semiconductor materials, being comparable to the values found for other bismuth halides studied as potential solar absorbers and optoelectronic materials, such as Cs_2AgBiX_6 ($X = Cl^-$ or Br^-).[19, 30, 49-50] Although this analysis is in accordance with the literature reported procedures and the obtained values are reasonable, the present case is different due to low dimensional crystal and electronic structures of $Rb_4Ag_2BiBr_9$. Thus, in $Rb_4Ag_2BiBr_9$, the frontier states originate from localized molecular states (arising from the isolated $BiBr_6$ octahedra), which produces flat bands (discussed below), favoring the formation of highly localized excitons. Therefore, the 2.82 eV absorption peak is attributed to excitonic absorption and the higher conduction band contains both Bi and Ag states that are mixed with Br-4p states, which yields the second absorption peak at 3.23 eV.

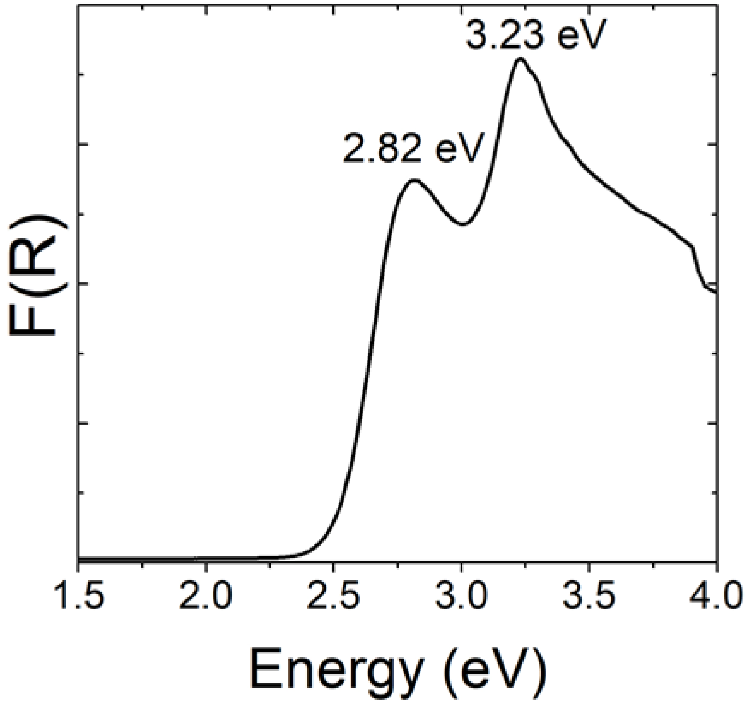

Figure 5. Kubelka-Munk function, F(R), plotted against photon energy converted from the diffuse reflectance data.

Under 3.815 eV UV irradiation, the room temperature PL spectrum of $Rb_4Ag_2BiBr_9$ (Figure 6a) shows a superposition of two emission bands; one weak, visible broadband emission (noted P1) centered at 2.36 eV, and another more intense, relatively narrow infrared emission band composed of multiple peaks noted P2, P3, and P4 located at 1.52, 1.44 and 1.28 eV, respectively. This weak and broad P1 emission is further consistent with an indirect transition or trap emission, similar to the emission reported for the isoelectronic trap AgBr:I,[54] and similar all-inorganic metal halides such as Cs_2AgBiX_6 (X = Br, Cl, I)[19, 30, 49-50] and $Cs_2AgInCl_6$.[55] To investigate the origin of the multiple-emission peaks, we measured the PLE spectra at 2.36 and 1.55 eV emission energies (Figure 6a). Notably, the PLE spectrum measured at 2.36 eV emission energy shows a broad peak at 3.34 eV, which is close to the 3.23 eV absorption peak shown in Figure 5. Moreover, the PLE spectrum measured at 1.55 eV emission energy shows a maximum at 2.82 eV, in excellent agreement with the low energy absorption peak observed from the optical absorption spectrum (Figure 5a). Therefore, we attribute the 3.23 and 2.82 eV absorption peaks to excitonic absorption primarily from two different species, $AgBr_5$ and $BiBr_6$ units. Electronic structure calculations (below) suggest that the exciton confined on $BiBr_6$ should have a lower energy than that on $AgBr_5$, which allows us to attribute the P1 emission peak to excitons localized on structural defect on $AgBr_5$ and the low energy P2, P3, and P4 emission lines to excitons localized on $BiBr_6$ octahedra. Note that several research works focused on the effect of the Bi^{3+} ion $6s^2$ doping alkaline-earth oxides such as CaO and SrO,[56-59] and wide band gap crystals like Cs_2NaYCl,[60] on the emission properties. For example, the PL spectra of Cs_2NaYCl activated with Bi^{3+} ions show vibrational structure and has been assigned to internal modes of $BiCl_6$ isolated octahedra.[60] Moreover, Pelle et al.[61] reported on the Bi^{3+} luminescence of $Cs_2NaBiCl_6$, that showed several bands in the red spectral region attributed to a strong coupling with the vibrational modes (strong exciton-phonon coupling). In the case of $Rb_4Ag_2BiBr_9$, the situation could be similar since the presence of isolated $BiBr_6$ octahedra may provide a strong exciton-phonon coupling which favors the possibility of STEs in structural defect within $BiBr_6$ blocks.

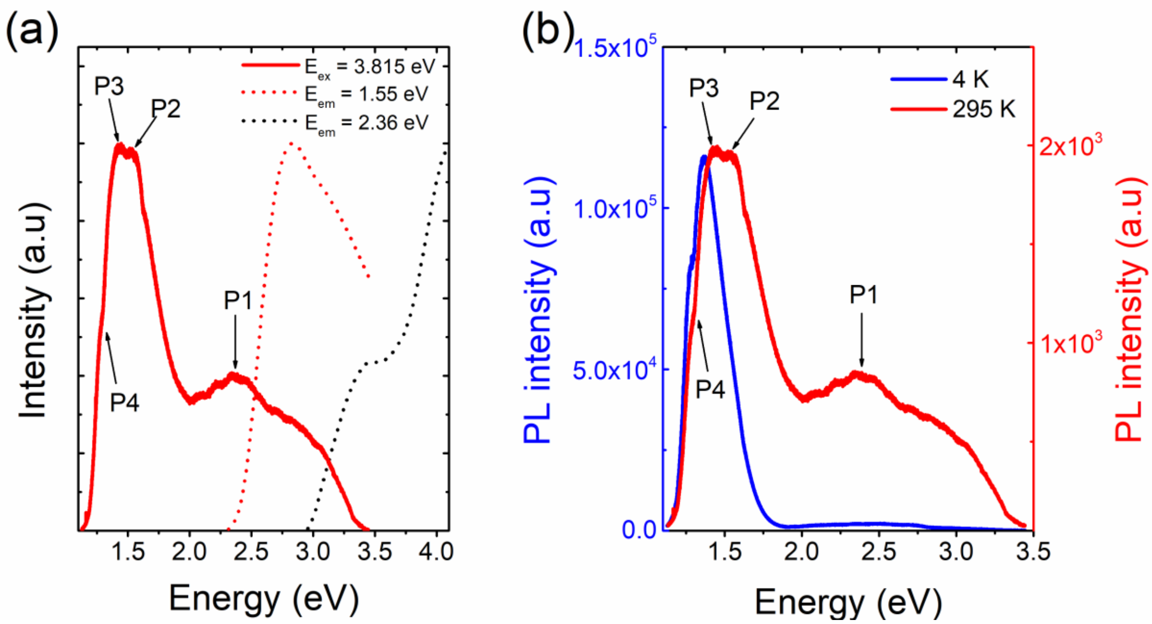

Figure 6. (a) Room temperature PL spectrum (red solid line) and PLE spectra measured for 1.55 (red dotted line) and 2.36 eV (black dotted line) emission energies. Plots of PL spectra measured at 4K (blue) and 295 K (red)of $Rb_4Ag_2BiBr_9$, under 3.815 eV irradiation.

Figure 6b shows the superposition of PL spectra measured at 4 K and room temperature. At 4 K, an enhancement (~2 orders of magnitude) of the low energy emission bands (P2, P3 and P4) was observed. In order to investigate the origin of the light emission of $Rb_4Ag_2BiBr_9$, we measured the temperature dependence of PL from 4 K to 295 K (Figures 7a and 7b). Significant changes were observed as a function of temperature. The intensity of P2, P3 and P4 PL peaks first increase as a function of temperature up to 100 K, then quench at higher temperature (Figure 7c). Similarly to the case of $Cs_{4-x}A_xSn(Br_{1-y}I_y)_6$ (A = Rb, K),[62] we attribute these low energy peaks to the presence of multiple self-trapped states, which could, in principle, result from a strong lattice coupling.[63-68] However, note that phase transitions between 100 K and room temperature has been ruled out by a single crystal XRD measurement performed at 100 K (see Table S3 in the SI), which confirmed that a normal contraction of unit cell volume occurs without any evidence for a structural transition. It is also possible that the multiple PL peaks in the emission spectrum may correspond to multiple indirect transitions,[19, 24-26, 30] or to defects or excitonic effects.[30] Moreover, the intensity of the high energy PL band (P1) shows a maximum at 175 K (Figure 7c).

Figure 7d shows the evolution of the intensities of P1-P4 PL peaks as a function of the excitation power, at ambient temperature. For P2-P4 peaks, its intensity shows a linear dependence with the excitation power, whereas a clear saturation was observed for P1 above 10 W/cm^2 excitation power. It is worth noting that the concentration and recombination lifetime for permanent defects are finite; thus, their PL could be saturated at high excitation power.[63-66, 69] Following the insights from electronic band structure calculations, the power dependence PL results and the discussion of the absorbance data above, we attribute this weak P1 emission to the presence of structural defects on Ag-Br units. Because the excitons on $AgBr_5$ have higher energy than that in $BiBr_6$, they relax to $BiBr_6$ and lead to the self-trapped exciton (STE) emission (peaks P2-4) at 4 K. With increasing temperature, the more mobile excitons on $AgBr_5$ are trapped by defects (e.g., on a Br vacancy adjacent to Ag), leading to a weaker P1 emission. The relaxation of defect-trapped excitons to $BiBr_6$ octahedra is prevented by the spatial separation of $BiBr_6$ units and defects on $AgBr_5$. Based on this explanation, the defect-bound exciton could be a metastable state with higher energy than the exciton bound to $BiBr_6$, thus explaining the broad nature of the P1 emission.

However, the trapping energy at the defect level may be larger than the self-trapping on $BiBr_6$, which could explain the fact that the thermal quenching for the STE emission (P2-4) starts from a lower temperature (100 K) compared to that for the defect (P1) emission (175 K).

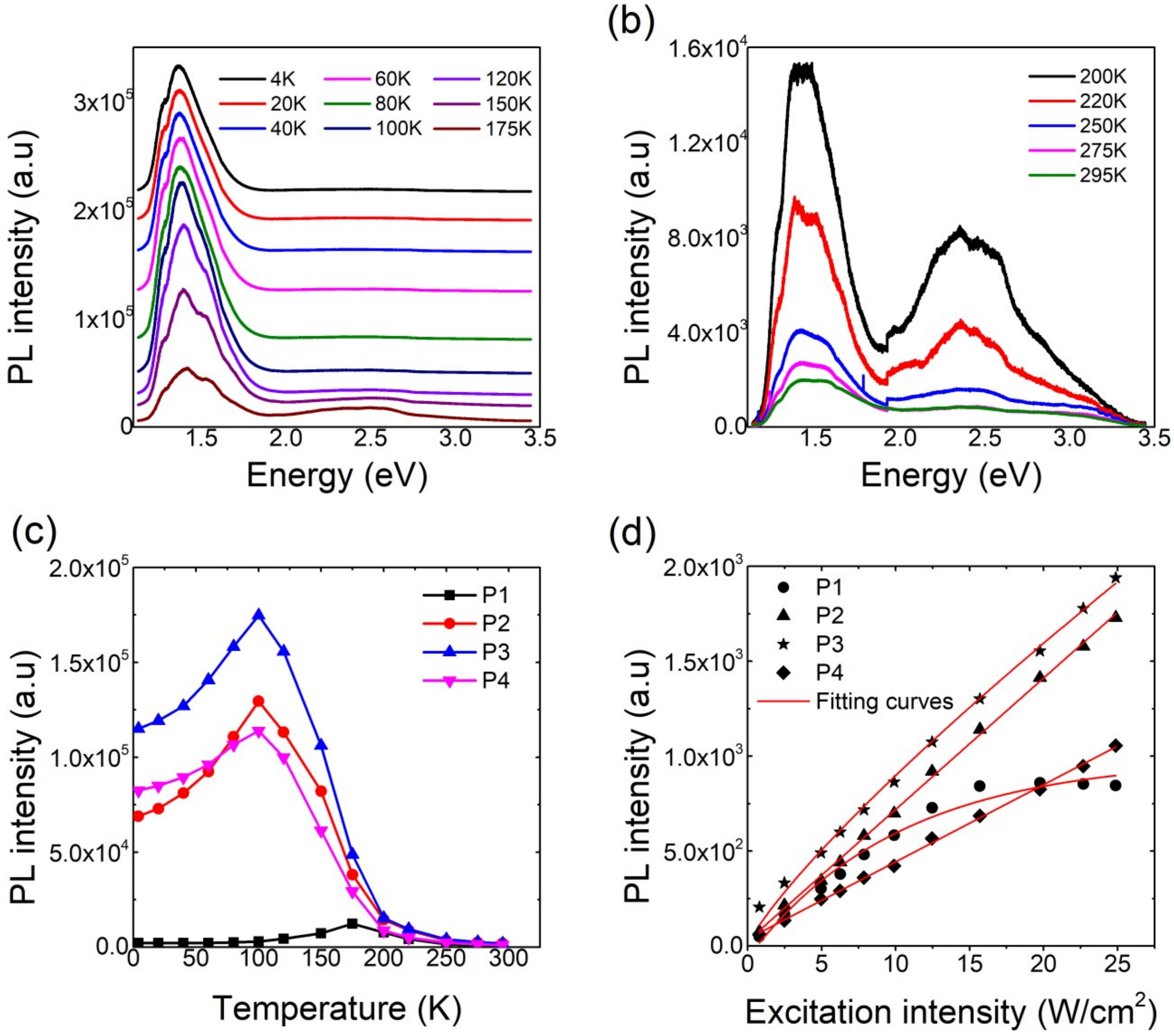

Figure 7. Temperature dependence PL spectra of $Rb_4Ag_2BiBr_9$ for the temperature range (a) [4-175 K] and (b) [200- 295 K] under 3.815 eV laser irradiation. Spectra are separated for clarity. (c) Plots of the intensity of PL peaks as a function of temperature. (d) Plots of the P1-P4 PL peaks intensity vs excitation power.

Electronic Band Structure Calculation. The calculated electronic band structure of $Rb_4Ag_2BiBr_9$ (including the SOC) is shown in Figure 8a. The band gap is slightly indirect. The indirect band gap of 1.69 eV (the valence and conduction band edges located at the U and S points, respectively) is larger than the direct band gap at the U point by less than 0.01 eV. Moreover, the calculated band structure of $Rb_4Ag_2BiBr_9$ is similar to that reported for all inorganic halides double perovskite, such as Cs_2AgBiX_6 ($X = Cl^-$ or Br^-)[19, 30, 49-50] and Cs_2AgTlX_6.[70]

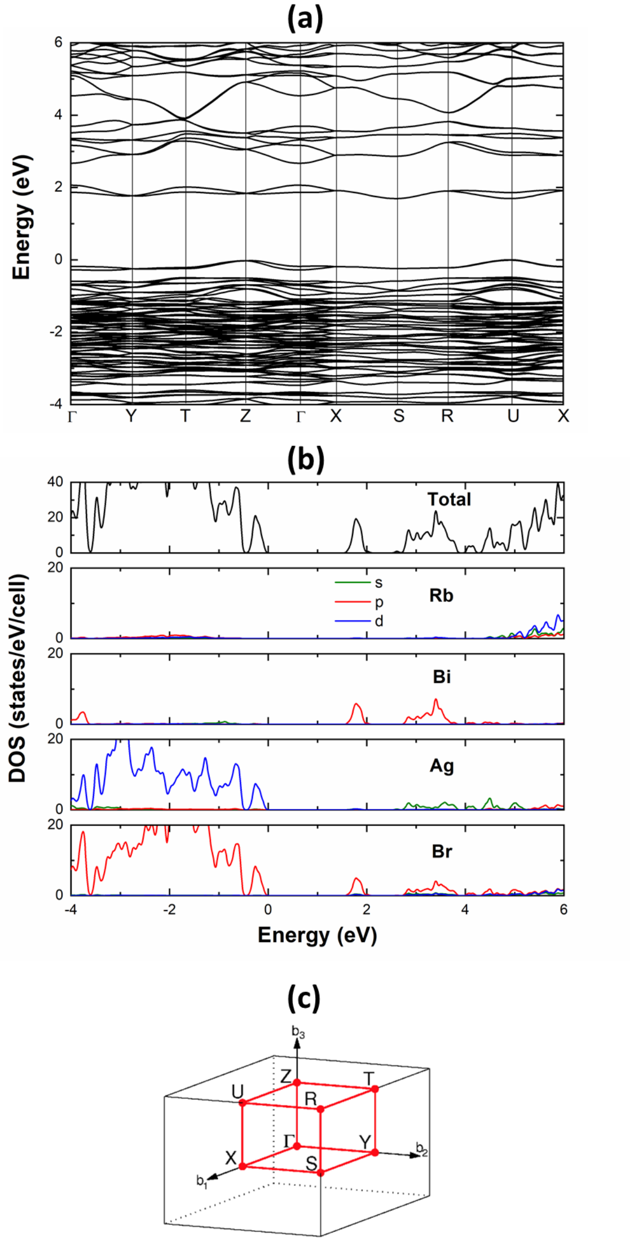

Figure 8. (a) Electronic band structures and (b) density of states (DOS) projected to each atomic species for $Rb_4Ag_2BiBr_9$ obtained using the PBE calculations including the spin-orbit coupling. (c) Plot of Brillouin zone with labels of high-symmetry k-points for $Rb_4Ag_2BiBr_9$. Note that the band gap is underestimated due to well-known band gap error in the PBE calculation.

The DOS projected onto each atomic species in Figure 8b shows that the conduction band has the mixed Bi-6p and Br-4p characters, while the valence band is made up of antibonding Br-4p and Ag-4d orbitals. The Bi-6p band is split as shown in Figure 8b by the SOC. Therefore, the composition of the bands around the Fermi level for $Rb_4Ag_2BiBr_9$ is largely similar to that reported for $Cs_2AgBiBr_6$,[19] which also exhibits a strong contribution from Bi-6p and smaller contribution from Br-4p to the conduction band and the valence band made of primarily Br-4p and Ag-4d states.

The $BiBr_6$ octahedra are not structurally connected, therefore, the Br-6p-derived conduction band states are spatially localized in $Rb_4Ag_2BiBr_9$, leading to small dispersion in the conduction band. Interestingly, this parallels the band structures of double perovskite halides, too. Thus, extensive theoretical calculations on model double perovskites such as Cs_2SrPbI_6 have shown that despite their nominal 3D crystal structures, elpasolites have effectively 0D electronic dimensionality with nondispersive valence (VB) and conduction (CB) bands.[71] In the present case, the wavefunction analysis of the $Rb_4Ag_2BiBr_9$ valence band shows that the hybridization between the Ag-4d and the Br-4p states are largely confined within the 2D plane perpendicular to the *a*-axis, indicating the quasi-2D nature of the electronic structure. The $AgBr_5$ square pyramids are connected through edge- and corner-sharing along the *b*-axis; thus, their electronic coupling along the *c*-axis is relatively weak. In addition, the Br-4p orbitals are polarized roughly along the *b*-axis for the corner-sharing Br ions but perpendicular to the *b*-axis for the edge-sharing Br ions, which reduces the electronic coupling along the *b*-axis. As a result, the valence band also has small dispersion, even along the directions parallel to the *bc* plane, as shown in Figure 8b. The localized electronic states on both $BiBr_6$ octahedra and $AgBr_5$ square pyramids should promote exciton localization. The optical excitation may create Bi- and Ag-centered localized excitons; the exciton on Bi should have the lower energy.

CONCLUSION

In summary, we prepared a new lead-free halide material $Rb_4Ag_2BiBr_9$, which is the first reported compound in the quaternary Rb-Ag-Bi-Br system. $Rb_4Ag_2BiBr_9$ crystallizes in a new structure type featuring alternating layers of $[Ag_2BiBr_9]^{4-}$ polyanions separated by Rb^+ cations. The $[Ag_2BiBr_9]^{4-}$ layers are made of octahedral $BiBr_6$ and square pyramidal $AgBr_5$ building blocks. There are elongated interlayer Ag-Br contacts that complete the Ag coordination environment to octahedral, invoking direct comparisons with Pb- and Bi-based halide perovskites.

Optical measurements and electronic structure calculations confirm parallels with the double perovskites such as $Cs_2AgBiBr_6$. Room temperature PL spectrum also contains multiple peaks located at 2.36 1.52, 1.44 and 1.28 eV, which are assigned to defects and self-trapped states. These values are comparable to the reported optical band gap at 2.21 eV and PL emission at 1.87 eV for the related $Cs_2AgBiBr_6$. The electronic structure calculations reveal that the band gap is slightly indirect with the calculated value of 1.69 eV. In agreement with the layered crystal structure, the nature of the electronic structure is also low dimensional with both CB and VB featuring flat bands. In fact, the band structure is more accurately described as 0D units of $BiBr_6$ and 1D chains of $AgBr_5$, overall yielding the quasi-2D nature of the electronic structure.

Based on our combined experimental and theoretical investigations of $Rb_4Ag_2BiBr_9$, the larger band gap above 2 eV coupled with flat bands in CB and VB represent major challenges for the utilization of this material in high-efficiency solar cells. However, this material and its isostructural variants may be considered for other optical and electronic applications. The related $Cs_2AgBiBr_6$ with an indirect large band gap of 2.1 eV and relatively flat bands in CB and VB[19] has been successfully incorporated into highly sensitive X-ray detector devices.[28-29] Similar to $Cs_2AgBiBr_6$, we were able to grow large-size crystals of $Rb_4Ag_2BiBr_9$ using a simple solution approach, which should simplify characterization of radiation detection properties of this material. Further studies on this front are currently ongoing. Moreover, thin films preparation of $Rb_4Ag_2BiBr_9$, and its morphology and optoelectronic characterization are under consideration and will be reported in a separate study. Finally, we are also currently working on the optimization of the optoelectronic properties (e.g., band gaps, luminescence properties, etc.) of $Rb_4Ag_2BiBr_9$, which represents a brand new class of halides with a new structure type, through chemical substitutions on halide anion and metal cation sites.

ASSOCIATED CONTENT

Supporting Information.

Tables with atomic coordinates, interatomic distances and bond angles, crystal structure figures, optical image of crystals, energy–dispersive X-ray measurements, powder X-ray diffraction patterns, and diffuse reflectance data.

AUTHOR INFORMATION

Corresponding Author

*E-mail: saparov@ou.edu

Note

The authors declare no competing financial interest.

Author Contributions

The manuscript was written through contributions of all authors. All authors have given approval to the final version of the manuscript. MS prepared the sample, performed the XRD measurements, and wrote the paper, AY carried out and analyzed the optical measurements and wrote the paper, VRW and IRS assisted on the photoluminescence measurements, DH, SC, and M-HD did the DFT calculations, and BS conceived the idea, wrote the paper and supervised the work. ‡MS and AY contributed equally to this work.

ACKNOWLEDGMENT

We acknowledge the financial support for this work provided by the University of Oklahoma startup funds and by a grant from Oklahoma Center for the Advancement of Science and Technology (OCAST) under grant AR18-008. M.-H. Du was supported by the U. S. Department of Energy, Office of Science, Basic Energy Sciences, Materials Sciences and Engineering Division. D. Han and S. Chen were supported by NSFC under Grant Nos. 61574059 and 61722402, Shu-Guang program (15SG20) and CC of ECNU. We thank Dr. Douglas R. Powell for his help with the single crystal X-ray diffraction measurements collected on instruments purchased using NSF grants CHE-1726630 and CHE-0130835. We also thank Mr. Benjamin Watkins for his assistance with our crystal growth experiments.

REFERENCES

1. Saparov, B.; Mitzi, D. B., Organic–Inorganic Perovskites: Structural Versatility for Functional Materials Design. *Chem. Rev.* **2016,** *116* (7), 4558-4596.
2. Protesescu, L.; Yakunin, S.; Bodnarchuk, M. I.; Krieg, F.; Caputo, R.; Hendon, C. H.; Yang, R. X.; Walsh, A.; Kovalenko, M. V., Nanocrystals of Cesium Lead Halide Perovskites (CsPbX3, X = Cl, Br, and I): Novel Optoelectronic Materials Showing Bright Emission with Wide Color Gamut. *Nano Letters* **2015,** *15* (6), 3692-3696.
3. Ye, H. Y.; Zhang, Y.; Fu, D. W.; Xiong, R. G., An Above-Room-Temperature Ferroelectric Organo–Metal Halide Perovskite: (3-Pyrrolinium)(CdCl3). *Angewandte Chemie International Edition* **2014,** *53* (42), 11242-11247.
4. Eperon, G. E.; Paternò, G. M.; Sutton, R. J.; Zampetti, A.; Haghighirad, A. A.; Cacialli, F.; Snaith, H. J., Inorganic caesium lead iodide perovskite solar cells. *Journal of Materials Chemistry A* **2015,** *3* (39), 19688-19695.
5. Manser, J. S.; Christians, J. A.; Kamat, P. V., Intriguing Optoelectronic Properties of Metal Halide Perovskites. *Chem. Rev.* **2016,** *116* (21), 12956-13008.
6. Kovalenko, M. V.; Protesescu, L.; Bodnarchuk, M. I., Properties and potential optoelectronic applications of lead halide perovskite nanocrystals. *Science* **2017,** *358* (6364), 745.
7. Eperon, G. E.; Burlakov, V. M.; Docampo, P.; Goriely, A.; Snaith, H. J., Morphological Control for High Performance, Solution-Processed Planar Heterojunction Perovskite Solar Cells. *Adv. Funct. Mater.* **2014,** *24* (1), 151-157.

8. Tan, Z.-K.; Moghaddam, R. S.; Lai, M. L.; Docampo, P.; Higler, R.; Deschler, F.; Price, M.; Sadhanala, A.; Pazos, L. M.; Credgington, D.; Hanusch, F.; Bein, T.; Snaith, H. J.; Friend, R. H., Bright light-emitting diodes based on organometal halide perovskite. *Nature Nanotechnology* **2014,** *9*, 687.
9. Wang, N.; Cheng, L.; Ge, R.; Zhang, S.; Miao, Y.; Zou, W.; Yi, C.; Sun, Y.; Cao, Y.; Yang, R.; Wei, Y.; Guo, Q.; Ke, Y.; Yu, M.; Jin, Y.; Liu, Y.; Ding, Q.; Di, D.; Yang, L.; Xing, G.; Tian, H.; Jin, C.; Gao, F.; Friend, R. H.; Wang, J.; Huang, W., Perovskite light-emitting diodes based on solution-processed self-organized multiple quantum wells. *Nature Photonics* **2016,** *10*, 699.
10. Yakunin, S.; Sytnyk, M.; Kriegner, D.; Shrestha, S.; Richter, M.; Matt, G. J.; Azimi, H.; Brabec, C. J.; Stangl, J.; Kovalenko, M. V.; Heiss, W., Detection of X-ray photons by solution-processed lead halide perovskites. *Nature Photonics* **2015,** *9*, 444.
11. Stoumpos, C. C.; Malliakas, C. D.; Kanatzidis, M. G., Semiconducting Tin and Lead Iodide Perovskites with Organic Cations: Phase Transitions, High Mobilities, and Near-Infrared Photoluminescent Properties. *Inorganic Chemistry* **2013,** *52* (15), 9019-9038.
12. Hao, F.; Stoumpos, C. C.; Cao, D. H.; Chang, R. P. H.; Kanatzidis, M. G., Lead-free solid-state organic–inorganic halide perovskite solar cells. *Nature Photonics* **2014,** *8*, 489.
13. Stoumpos, C. C.; Frazer, L.; Clark, D. J.; Kim, Y. S.; Rhim, S. H.; Freeman, A. J.; Ketterson, J. B.; Jang, J. I.; Kanatzidis, M. G., Hybrid Germanium Iodide Perovskite Semiconductors: Active Lone Pairs, Structural Distortions, Direct and Indirect Energy Gaps, and Strong Nonlinear Optical Properties. *Journal of the American Chemical Society* **2015,** *137* (21), 6804-6819.
14. Ganose, A. M.; Savory, C. N.; Scanlon, D. O., Beyond methylammonium lead iodide: prospects for the emergent field of ns2 containing solar absorbers. *Chem Commun* **2017,** *53* (1), 20-44.
15. Lyu, M.; Yun, J.-H.; Chen, P.; Hao, M.; Wang, L., Addressing Toxicity of Lead: Progress and Applications of Low-Toxic Metal Halide Perovskites and Their Derivatives. *Adv. Energy Mater.* **2017,** *7* (15), 1602512.
16. Lyu, M.; Yun, J.-H.; Cai, M.; Jiao, Y.; Bernhardt, P. V.; Zhang, M.; Wang, Q.; Du, A.; Wang, H.; Liu, G.; Wang, L., Organic–inorganic bismuth (III)-based material: A lead-free, air-stable and solution-processable light-absorber beyond organolead perovskites. *Nano Research* **2016,** *9* (3), 692-702.
17. Öz, S.; Hebig, J.-C.; Jung, E.; Singh, T.; Lepcha, A.; Olthof, S.; Jan, F.; Gao, Y.; German, R.; van Loosdrecht, P. H. M.; Meerholz, K.; Kirchartz, T.; Mathur, S., Zero-dimensional (CH3NH3)3Bi2I9 perovskite for optoelectronic applications. *Solar Energy Materials and Solar Cells* **2016,** *158*, 195-201.
18. Slavney, A. H.; Leppert, L.; Bartesaghi, D.; Gold-Parker, A.; Toney, M. F.; Savenije, T. J.; Neaton, J. B.; Karunadasa, H. I., Defect-Induced Band-Edge Reconstruction of a Bismuth-Halide Double Perovskite for Visible-Light Absorption. *Journal of the American Chemical Society* **2017,** *139* (14), 5015-5018.
19. McClure, E. T.; Ball, M. R.; Windl, W.; Woodward, P. M., Cs2AgBiX6 (X = Br, Cl): New Visible Light Absorbing, Lead-Free Halide Perovskite Semiconductors. *Chem. Mater.* **2016,** *28* (5), 1348-1354.
20. Saparov, B.; Hong, F.; Sun, J.-P.; Duan, H.-S.; Meng, W.; Cameron, S.; Hill, I. G.; Yan, Y.; Mitzi, D. B., Thin-Film Preparation and Characterization of Cs3Sb2I9: A Lead-Free Layered Perovskite Semiconductor. *Chemistry of Materials* **2015,** *27* (16), 5622-5632.

21. Liang, J.; Wang, C.; Wang, Y.; Xu, Z.; Lu, Z.; Ma, Y.; Zhu, H.; Hu, Y.; Xiao, C.; Yi, X.; Zhu, G.; Lv, H.; Ma, L.; Chen, T.; Tie, Z.; Jin, Z.; Liu, J., All-Inorganic Perovskite Solar Cells. *Journal of the American Chemical Society* **2016,** *138* (49), 15829-15832.
22. Kulbak, M.; Gupta, S.; Kedem, N.; Levine, I.; Bendikov, T.; Hodes, G.; Cahen, D., Cesium Enhances Long-Term Stability of Lead Bromide Perovskite-Based Solar Cells. *The Journal of Physical Chemistry Letters* **2016,** *7* (1), 167-172.
23. Liang, J.; Zhao, P.; Wang, C.; Wang, Y.; Hu, Y.; Zhu, G.; Ma, L.; Liu, J.; Jin, Z., CsPb0.9Sn0.1IBr2 Based All-Inorganic Perovskite Solar Cells with Exceptional Efficiency and Stability. *Journal of the American Chemical Society* **2017,** *139* (40), 14009-14012.
24. Volonakis, G.; Filip, M. R.; Haghighirad, A. A.; Sakai, N.; Wenger, B.; Snaith, H. J.; Giustino, F., Lead-Free Halide Double Perovskites via Heterovalent Substitution of Noble Metals. *The Journal of Physical Chemistry Letters* **2016,** *7* (7), 1254-1259.
25. Filip, M. R.; Hillman, S.; Haghighirad, A. A.; Snaith, H. J.; Giustino, F., Band Gaps of the Lead-Free Halide Double Perovskites Cs2BiAgCl6 and Cs2BiAgBr6 from Theory and Experiment. *The Journal of Physical Chemistry Letters* **2016,** *7* (13), 2579-2585.
26. Savory, C. N.; Walsh, A.; Scanlon, D. O., Can Pb-Free Halide Double Perovskites Support High-Efficiency Solar Cells? *ACS Energy Letters* **2016,** *1* (5), 949-955.
27. Kentsch, R.; Scholz, M.; Horn, J.; Schlettwein, D.; Oum, K.; Lenzer, T., Exciton Dynamics and Electron–Phonon Coupling Affect the Photovoltaic Performance of the Cs2AgBiBr6 Double Perovskite. *J. Phys. Chem. C* **2018,** *122* (45), 25940-25947.
28. Steele, J. A.; Pan, W.; Martin, C.; Keshavarz, M.; Debroye, E.; Yuan, H.; Banerjee, S.; Fron, E.; Jonckheere, D.; Kim, C. W.; Baekelant, W.; Niu, G.; Tang, J.; Vanacken, J.; Van der Auweraer, M.; Hofkens, J.; Roeffaers, M. B. J., Photophysical Pathways in Highly Sensitive Cs2AgBiBr6 Double-Perovskite Single-Crystal X-Ray Detectors. *Adv. Mater.* **2018,** *0* (0), 1804450.
29. Pan, W.; Wu, H.; Luo, J.; Deng, Z.; Ge, C.; Chen, C.; Jiang, X.; Yin, W.-J.; Niu, G.; Zhu, L.; Yin, L.; Zhou, Y.; Xie, Q.; Ke, X.; Sui, M.; Tang, J., Cs2AgBiBr6 single-crystal X-ray detectors with a low detection limit. *Nat. Photonics* **2017,** *11* (11), 726-732.
30. Slavney, A. H.; Hu, T.; Lindenberg, A. M.; Karunadasa, H. I., A Bismuth-Halide Double Perovskite with Long Carrier Recombination Lifetime for Photovoltaic Applications. *J. Am. Chem. Soc.* **2016,** *138* (7), 2138-2141.
31. Bruker, A.; SAINT, A., Inc., Madison, WI, 2004 Search PubMed;(b) GM Sheldrick. *Acta Crystallogr., Sect. A: Fundam. Crystallogr* **2008,** *64*, 112.
32. Gelato, L. M.; Parthe, E., STRUCTURE TIDY - a computer program to standardize crystal structure data. *Journal of Applied Crystallography* **1987,** *20* (2), 139-143.
33. *The Rigaku Journal* **2010,** *26* (1).
34. Kresse, G.; Furthmüller, J., Efficiency of ab-initio total energy calculations for metals and semiconductors using a plane-wave basis set. *Computational Materials Science* **1996,** *6* (1), 15-50.
35. Kresse, G.; Joubert, D., From ultrasoft pseudopotentials to the projector augmented-wave method. *Physical Review B* **1999,** *59* (3), 1758.
36. Perdew, J. P.; Burke, K.; Ernzerhof, M., Generalized gradient approximation made simple. *Physical review letters* **1996,** *77* (18), 3865.
37. Wei, F.; Deng, Z.; Sun, S.; Zhang, F.; Evans, D. M.; Kieslich, G.; Tominaka, S.; Carpenter, M. A.; Zhang, J.; Bristowe, P. D.; Cheetham, A. K., Synthesis and Properties of a Lead-

Free Hybrid Double Perovskite: (CH3NH3)2AgBiBr6. *Chemistry of Materials* **2017,** *29* (3), 1089-1094.

38. Shannon, R., Revised Effective Ionic Radii and Systematic Studies of Interatomic Distances in Halides and Chalcogenides. *Acta Crystallographica Section A* **1976,** *32* (5), 751-767.
39. Ag3Bi14Br21: ein Subbromid mit Bi24+-Hanteln und Bi95+-Polyedern – Synthese, Kristallstruktur und Chemische Bindung. *Zeitschrift für anorganische und allgemeine Chemie* **2008,** *634* (15), 2873-2879.
40. Yue, C.-Y.; Lei, X.-W.; Han, Y.-F.; Lu, X.-X.; Tian, Y.-W.; Xu, J.; Liu, X.-F.; Xu, X., Transition-Metal-Complex Cationic Dyes Photosensitive to Two Types of 2D Layered Silver Bromides with Visible-Light-Driven Photocatalytic Properties. *Inorganic Chemistry* **2016,** *55* (23), 12193-12203.
41. Slavney, A. H.; Smaha, R. W.; Smith, I. C.; Jaffe, A.; Umeyama, D.; Karunadasa, H. I., Chemical Approaches to Addressing the Instability and Toxicity of Lead–Halide Perovskite Absorbers. *Inorg. Chem.* **2017,** *56* (1), 46-55.
42. Kim, J.; Yun, J. S.; Cho, Y.; Lee, D. S.; Wilkinson, B.; Soufiani, A. M.; Deng, X.; Zheng, J.; Shi, A.; Lim, S.; Chen, S.; Hameiri, Z.; Zhang, M.; Lau, C. F. J.; Huang, S.; Green, M. A.; Ho-Baillie, A. W. Y., Overcoming the Challenges of Large-Area High-Efficiency Perovskite Solar Cells. *ACS Energy Lett.* **2017,** *2* (9), 1978-1984.
43. Brunetti, B.; Cavallo, C.; Ciccioli, A.; Gigli, G.; Latini, A., On the Thermal and Thermodynamic (In)Stability of Methylammonium Lead Halide Perovskites. *Sci. Rep.* **2016,** *6*, 31896.
44. Baranwal, A. K.; Kanaya, S.; Peiris, T. A. N.; Mizuta, G.; Nishina, T.; Kanda, H.; Miyasaka, T.; Segawa, H.; Ito, S., 100 °C Thermal Stability of Printable Perovskite Solar Cells Using Porous Carbon Counter Electrodes. *ChemSusChem* **2016,** *9* (18), 2604-2608.
45. Zhao, X.; Park, N.-G., Stability Issues on Perovskite Solar Cells. *Photonics* **2015,** *2* (4), 1139.
46. Bag, M.; Renna, L. A.; Adhikari, R. Y.; Karak, S.; Liu, F.; Lahti, P. M.; Russell, T. P.; Tuominen, M. T.; Venkataraman, D., Kinetics of Ion Transport in Perovskite Active Layers and Its Implications for Active Layer Stability. *J. Am. Chem. Soc.* **2015,** *137* (40), 13130-13137.
47. Eames, C.; Frost, J. M.; Barnes, P. R. F.; O'Regan, B. C.; Walsh, A.; Islam, M. S., Ionic transport in hybrid lead iodide perovskite solar cells. *Nat. Commun.* **2015,** *6*, 7497.
48. Roccanova, R.; Ming, W.; Whiteside, V. R.; McGuire, M. A.; Sellers, I. R.; Du, M.-H.; Saparov, B., Synthesis, Crystal and Electronic Structures, and Optical Properties of $(CH_3NH_3)_2CdX_4$ (X = Cl, Br, I). *Inorg. Chem.* **2017,** *56* (22), 13878-13888.
49. Creutz, S. E.; Crites, E. N.; De Siena, M. C.; Gamelin, D. R., Colloidal Nanocrystals of Lead-Free Double-Perovskite (Elpasolite) Semiconductors: Synthesis and Anion Exchange To Access New Materials. *Nano Lett.* **2018,** *18* (2), 1118-1123.
50. Bekenstein, Y.; Dahl, J. C.; Huang, J.; Osowiecki, W. T.; Swabeck, J. K.; Chan, E. M.; Yang, P.; Alivisatos, A. P., The Making and Breaking of Lead-Free Double Perovskite Nanocrystals of Cesium Silver–Bismuth Halide Compositions. *Nano Lett.* **2018,** *18* (6), 3502-3508.
51. Yogamalar, N. R.; Chandra Bose, A., Burstein–Moss shift and room temperature near-band-edge luminescence in lithium-doped zinc oxide. *Appl Phys A* **2011,** *103* (1), 33-42.

52. Zachary, M. G.; Aaron, L.; Snyder, G. J., Optical band gap and the Burstein–Moss effect in iodine doped PbTe using diffuse reflectance infrared Fourier transform spectroscopy. *New J. Phys.* **2013,** *15* (7), 075020.
53. Tauc, J.; Grigorovici, R.; Vancu, A., Optical Properties and Electronic Structure of Amorphous Germanium. *phys. status solidi (b)* **1966,** *15* (2), 627-637.
54. Czaja, W.; Baldereschi, A., The isoelectronic trap iodine in AgBr. *J. Phys. C: Solid State Phys.* **1979,** *12* (2), 405.
55. Locardi, F.; Cirignano, M.; Baranov, D.; Dang, Z.; Prato, M.; Drago, F.; Ferretti, M.; Pinchetti, V.; Fanciulli, M.; Brovelli, S.; De Trizio, L.; Manna, L., Colloidal Synthesis of Double Perovskite Cs2AgInCl6 and Mn-Doped Cs2AgInCl6 Nanocrystals. *J. Am. Chem. Soc.* **2018,** *140* (40), 12989-12995.
56. van der Steen, A. C.; Dijcks, L. T. F., The Luminescence Properties of Alkaline-Earth Oxides Activated with 6s2 Ions. *phys. status solidi (b)* **1981,** *104* (1), 283-292.
57. Oomen, E. W. J. L.; Dirksen, G. J.; Smit, W. M. A.; Blasse, G., On the luminescence of the Sb 3+ ion in Cs 2 NaMBr 6 (M=Sc,Y,La). *Journal of Physics C: Solid State Physics* **1987,** *20* (8), 1161.
58. Blasse, G.; van der Steen, A. C., Luminescence characteristics of Bi3+-activated oxides. *Solid State Commun.* **1979,** *31* (12), 993-994.
59. Jin, Y.; Hu, Y.; Chen, L.; Wang, X.; Ju, G.; Mu, Z., Persistent luminescence in Bi3+ doped CaWO4 matrix. *Radiat Meas* **2013,** *51-52*, 18-24.
60. Van Steen, A. C. D., Luminescence of Cs2NaYCl6—Bi3+ (6s2). *phys. status solidi (b)* **1980,** *100* (2), 603-611.
61. Pelle, F.; Jacquier, B.; Denis, J. P.; Blanzat, B., Optical properties of Cs2NaBiCl6. *J. Lumin.* **1978,** *17* (1), 61-72.
62. Benin, B. M.; Dirin, D. N.; Morad, V.; Wörle, M.; Yakunin, S.; Rainò, G.; Nazarenko, O.; Fischer, M.; Infante, I.; Kovalenko, M. V., Highly Emissive Self-Trapped Excitons in Fully Inorganic Zero-Dimensional Tin Halides. *Angew. Chem. Int. Ed.* **2018,** *57* (35), 11329-11333.
63. Fugol, I. Y., EXCITONS IN RARE-GAS CRYSTALS. *Adv. Phys.* **1978,** *27* (1), 1-87.
64. Williams, R. T.; Song, K. S., The self-trapped exciton. *J. Phys. Chem. Solids* **1990,** *51* (7), 679-716.
65. Yangui, A.; Garrot, D.; Lauret, J. S.; Lusson, A.; Bouchez, G.; Deleporte, E.; Pillet, S.; Bendeif, E. E.; Castro, M.; Triki, S.; Abid, Y.; Boukheddaden, K., Optical Investigation of Broadband White-Light Emission in Self-Assembled Organic–Inorganic Perovskite (C6H11NH3)2PbBr4. *J. Phys. Chem. C* **2015,** *119* (41), 23638-23647.
66. Yangui, A.; Pillet, S.; Bendeif, E.-E.; Lusson, A.; Triki, S.; Abid, Y.; Boukheddaden, K., Broadband Emission in a New Two-Dimensional Cd-Based Hybrid Perovskite. *ACS Photonics* **2018,** *5* (4), 1599-1611.
67. Yangui, A.; Pillet, S.; Lusson, A.; Bendeif, E. E.; Triki, S.; Abid, Y.; Boukheddaden, K., Control of the White-Light Emission in the Mixed Two-Dimensional Hybrid Perovskites (C6H11NH3)2[PbBr4–xIx]. *J. Alloys Compd.* **2017,** *699*, 1122.
68. Yangui, A.; Pillet, S.; Mlayah, A.; Lusson, A.; Bouchez, G.; Triki, S.; Abid, Y.; Boukheddaden, K., Structural phase transition causing anomalous photoluminescence behavior in perovskite (C6H11NH3)2[PbI4]. *J. Chem. Phys.* **2015,** *143* (22), 224201.
69. Reshchikov, M. A.; Morkoç, H., Luminescence properties of defects in GaN. *J. Appl. Phys.* **2005,** *97* (6), 061301.

70. Slavney, A. H.; Leppert, L.; Saldivar Valdes, A.; Bartesaghi, D.; Savenije, T. J.; Neaton, J. B.; Karunadasa, H. I., Small-Band-Gap Halide Double Perovskites. *Angew. Chem. Int. Ed.* **2018,** *57* (39), 12765-12770.
71. Xiao, Z.; Meng, W.; Wang, J.; Mitzi, D. B.; Yan, Y., Searching for promising new perovskite-based photovoltaic absorbers: the importance of electronic dimensionality. *Materials Horizons* **2017,** *4* (2), 206-216.

For Table of Contents Only

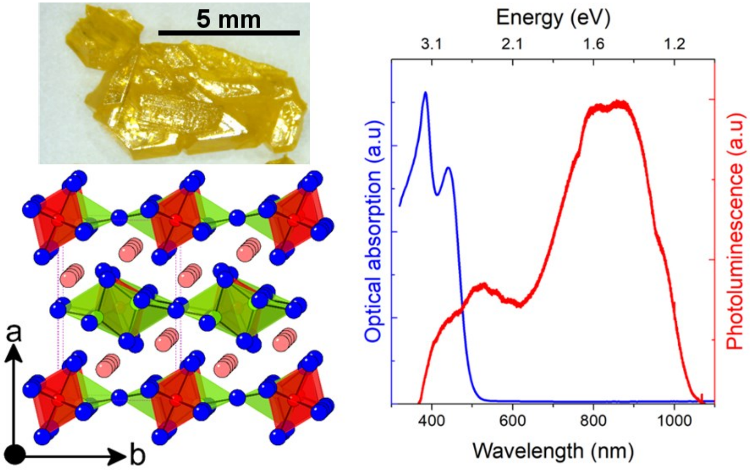

Synopsis

$Rb_4Ag_2BiBr_9$ is a new nontoxic, thermally and air stable lead-free all-inorganic semiconductor prepared using the mixed-cation approach. $Rb_4Ag_2BiBr_9$ adopts a new structure type featuring $BiBr_6$ octahedra and $AgBr_5$ square pyramids that share common edges and corners to form a unique 2D layered non-perovskite structure. Optical absorption measurements and electronic structure calculations suggest a nearly direct band gap for $Rb_4Ag_2BiBr_9$. Our theoretical and experimental studies suggest coexistence of defect-bound excitons and self-trapped excitons in $Rb_4Ag_2BiBr_9$.